



Drying of gypsum plaster prisms: prevention of visible sodium sulfate efflorescence through calcium formate addition

Nicholas Fobbe · Friedlinde Goetz-Neunhoeffler · Sebastian Foerthner · Henning Foerster · Daniel Jansen

Received: 20 February 2023 / Accepted: 17 July 2023 / Published online: 1 August 2023
© The Author(s) 2023

Abstract In this work, we investigated the drying process of a hardened gypsum plaster model (GP) that showed sodium sulfate efflorescence after subsequent exposure to water. Visible efflorescence could be prevented by adding small amounts of calcium formate (CF). Prism samples were prepared to investigate this observation, with an emphasis on chemical processes in the pore water. In the pure plaster, both sodium and sulfur accumulate at the surface of the prism, which leads to sodium sulfate precipitation. In the sample containing CF, calcium slightly accumulates at the surface, which leads to lower sulfur concentrations, because the porewater is in equilibrium with gypsum. Thermodynamic calculations show that higher sodium concentrations are then necessary to reach sodium sulfate supersaturation than without CF. These concentrations are not exceeded during early stages of the drying process, which ultimately leads to the sodium sulfate precipitation inside the prism. Therefore, sodium sulfate efflorescence can be hindered on gypsum plaster by the addition of CF.

Keywords Gypsum plaster · Sodium sulfate · Salt damage · Efflorescence · Thermodynamic modelling

1 Introduction

The crystallization of soluble salts in porous mineralogical building materials is a main mechanism in the surface deterioration of buildings. It causes the widespread decay of cultural heritage as well as of modern buildings. It is therefore of great cultural and economic interest to better understand the mechanisms behind these salt weathering processes. In general, salt damage occurs due to the subsequent wetting of hardened building material when water is highly saturated with dissolved ions. When the building material then dries and the water evaporates, ions accumulate, leading to the precipitation of soluble salts. If the crystallization pressure exceeds the tensile strength of the stone, the matrix fails and cracks form [1–6].

In gypsum plasters, the phenomenon of subsequent wetting usually leads to the formation of efflorescence. This is due to the fact that gypsum plasters have large average pore sizes and a high porosity (41–65%, [7]) compared to Portland cements (around 30%, [8]), which enables pore water to move easily to the surface of the body, thereby transporting dissolved ions. Due to the solubility of gypsum ($\text{CaSO}_4 \cdot 2\text{H}_2\text{O}$) of approx. 15 mmol/L in water at 25 °C, gypsum plasters are

N. Fobbe (✉) · F. Goetz-Neunhoeffler · D. Jansen
Geozentrum Nordbayern, Mineralogie, Friedrich-Alexander-Universität Erlangen-Nürnberg, Schlossgarten 5a, 91054 Erlangen, Germany
e-mail: nicholas.fobbe@fau.de

S. Foerthner · H. Foerster
Knauf Gips KG, Am Bahnhof 7, 97346 Iphofen, Germany



normally only used in the interior of buildings, where they are not exposed to wet weather conditions. However, they can still be damaged by subsequent watering, for example, if they are applied before the construction site is sealed, or due to pipe bursts or flooding events.

In comparison with other salts, the secondary crystallization of sodium sulfates is considered to be the most damaging to the building material. At room temperature, there are two stable phases: the anhydrous phase thenardite (Na_2SO_4) and decahydrate mirabilite ($\text{Na}_2\text{SO}_4 \cdot 10\text{H}_2\text{O}$). Generally, the severe damage inflicted upon the building material is caused by conversion from thenardite to the water-richer mirabilite. This process is dependent on the environmental conditions (relative humidity (RH) and temperature), which will be examined in more detail in the discussion [9–11].

In gypsum plasters, the occurrence of sodium sulfates as efflorescence can be countered with the addition of small amounts of calcium formate (CF). CF is a highly soluble salt that is known to accelerate the setting of Portland cement by accelerating the formation of ettringite and the silicate reaction during hydration [12, 13]. The hydration of bassanite is retarded by CF addition [14].

However, the contribution of CF to strengthening the resistance of gypsum plaster to subsequent sodium sulfate efflorescence crystallization has not been investigated yet. The aim of this paper is to analyze the beneficial influence of CF on the drying process of a gypsum plaster model that shows sodium sulfate efflorescence and to define the mechanism that prevents it. The focus lies on the pore water composition and thermodynamic interdependencies of mineral phases.

To cross-link the interdependencies of sodium concentrations, gypsum solubility, and sodium sulfate solubilities, solubility curves were calculated where the single ions of the phases varied independently of one another. This makes it possible to show “concentration paths” of the relevant ions and to easily comprehend the influence of calcium formate on pore water composition, the gypsum solubility, and the potential prevention of sodium sulfate efflorescence.

2 Materials and methods

Two sample series are investigated in this work. The first one is the base mix of the gypsum plaster model (GP) without any organic additions. The second one is the same gypsum plaster with an addition of 0.5 wt% CF (GP-CF). All experiments were repeated three times and carried out with deionized water at 23 ± 1 °C.

2.1 Gypsum plaster powder

The phase composition of the raw powder was evaluated by X-ray diffraction (XRD), using the Rietveld refinement method. It can be applied under the assumption, that all phases in a powder mixture are crystalline. For further information about this quantification method, the reader is referred to [8, 15]. The powder samples were prepared in Bruker standard powder specimen holders with 25 mm diameter, and the surface was flattened with a glass spar. The measurements were carried out in a Bruker D8 Advance device with Bragg–Brentano geometry and a LYNXEYE detector. The used radiation was $\text{CuK}\alpha$, and voltage and current were set to 40 kV and 40 mA, respectively. The step size was set to 0.011 ° 2θ , the counting time was 0.6 s/step and the detection range 7–70 ° 2θ . The structures used for the refinement and mineral formulas can be found in Table 1.

2.2 Prism preparation

Prism bodies of the two sample series were prepared with dimensions of $40 \times 40 \times 160$ mm (Fig. 1). The raw powder was mixed with water at a water/solid ratio of 0.8. After one minute, the paste was filled in the prism forms, where it remained for about one hour. At this time, the bodies were steady enough to be safely removed from the forms without breaking apart. They were then stored for another three hours at room temperature to ensure a complete hydration reaction of the gypsum plaster. Next, they were put in a 40 °C oven, where they were dried completely until mass constancy was reached.

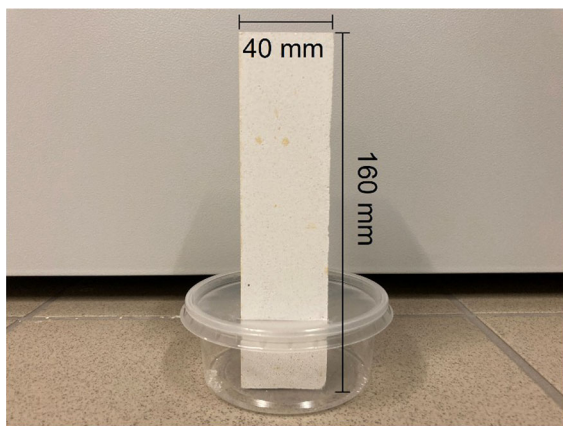
2.3 Efflorescence experiments

Efflorescence experiments were performed with the prism bodies using a similar set-up of methods as



Table 1 Crystal structures used for the TOPAS refinement of the efflorescence characterization

| Mineral | Formula | PDF number | References |
|-----------------|---|------------|------------|
| Bassanite | $\text{CaSO}_4 \cdot 0.5\text{H}_2\text{O}$ | 83-0439 | [17] |
| Anhydrite | CaSO_4 | 72-0916 | [18] |
| Calcite | CaCO_3 | 83-0577 | [19] |
| Polyhalite | $\text{K}_2\text{Ca}_2\text{Mg}(\text{SO}_4)_4 \cdot 2\text{H}_2\text{O}$ | 70-2157 | [20] |
| Thenardite | Na_2SO_4 | 74-2036 | [21] |
| Celestine | SrSO_4 | 74-2035 | [21] |
| Gypsum | $\text{CaSO}_4 \cdot 2\text{H}_2\text{O}$ | 70-0982 | [22] |
| Mirabilite | $\text{Na}_2\text{SO}_4 \cdot 10\text{H}_2\text{O}$ | 11-0647 | [23] |
| Glauberite | $\text{CaNa}_2(\text{SO}_4)_2$ | 72-1375 | [24] |
| Shortite | $\text{Ca}_2\text{Na}_2(\text{CO}_3)_3$ | 72-1026 | [25] |
| Calcium formate | $\text{Ca}(\text{HCOO})_2$ | 14-0819 | [26] |
| Sodium formate | $\text{Na}(\text{HCOO})$ | 14-0812 | [27] |
| Quartz | SiO_2 | 05-0490 | [28] |
| Anorthite | $\text{CaAl}_2(\text{SiO}_4)_2$ | 75-1587 | [29] |

**Fig. 1** Prism with dimensions of $40 \times 40 \times 160$ mm

published in [16], where a flue gas desulfurization gypsum that showed hexahydrate ($\text{MgSO}_4 \cdot 6\text{H}_2\text{O}$) efflorescence was investigated. The prism bodies were put into beakers filled with 100 mL water. However, this time the prisms were not masked with adhesive tape. They were partially sealed by the lids of the beakers, equaling the surface to volume ratio of the prisms in practical applications (Fig. 1) when the gypsum plaster layer on the wall is one centimeter thick. Free space between prisms and lids were sealed with parafilm to reduce evaporation in the intersection. The prisms were stored in a KBF 115 climate chamber from BINDER GmbH at 23 ± 0.2 °C and $50 \pm 2\%$ relative humidity (RH). The drying rate of the prisms was observed by repeated weighing. After

drying times of 3, 6, 12, and 18 h, the pore water was pressed out of the prisms with a hydraulic press for further investigations (see Chapter 2.5 for details).

2.4 Efflorescence characterization

To characterize the mineralogical composition of the efflorescence and to check whether formate salts grow on GP-CF samples, XRD measurements were carried out in a Bruker D8 advance device with Bragg-Brentano geometry, similar to the raw powder characterization (Sect. 2.1). The material was scratched off the prism and then put on a silicon sample carrier that is cut so that no reflexes emerge in the XRD diagram. Some desiccator grease was put on the sample carrier, and the material was then spread over it. The software TOPAS was used to analyze the measured diagram, and Table 1 shows the structures used for the refinement, with the ICSD database.

2.5 Pore water analysis

The pore water was analyzed after 3, 6, 12, and 18 h. To comprehend ion movements through the prisms, they were cut into three equally sized pieces at 5.3 and 10.6 cm prism heights (Fig. 2). They were then put in a Stuermer Metallkraft hydraulic press of type WPP30. The pore water was pressed out of each prism piece with a maximum pressure of 400 bar and subsequently filtered through a $0.2 \mu\text{m}$ syringe filter. To stabilize the pore water composition and avoid

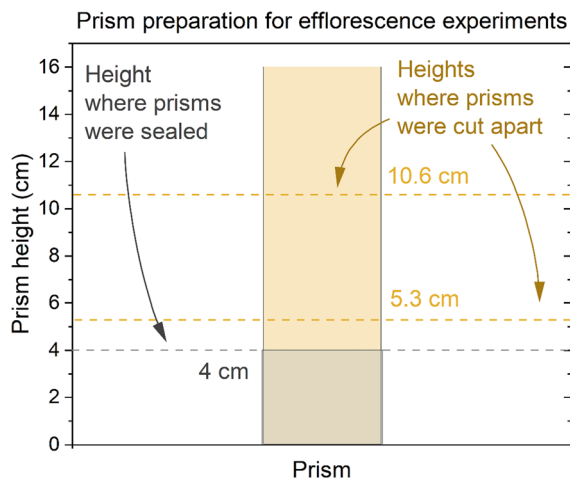


Fig. 2 Preparation of the prisms for the efflorescence experiments

precipitation of phases, HNO_3 was added to the samples in the ratio 2/1 (pore water/ HNO_3). For the samples after 12 and 18 h, only the top prism pieces were analyzed.

Major anions (F^- , Br^- , Cl^- , NO_3^- , NO_2^- , SO_4^{2-} , PO_4^{3-}) were determined by ion chromatography (ICS 2000, Thermo Dionex). The limit for the quantification of major ions was 0.1 mg/L with a typical precision of < 5% relative standard deviation (RSD) based on the repeated analysis of two control standards treated as unknowns in the lower and upper calibration range. Major cations (Na^+ , K^+ , Li^+ , NH_4^+ , Ca^{2+} , Fe^{2+} , Mg^{2+}) and trace elements were analyzed using a iCAP Qc ICP-MS (Thermo Fisher Scientific Inc.) fed by a SC-2DXS autosampler (Elemental Scientifics). Samples were measured three times. The typical RSD for three replicates was better than 1%. For most elements, the practical quantification limit is 0.1 $\mu\text{g/L}$. Operating conditions of the instrument are reported in Table 2.

Water samples were furthermore analyzed for the carbon stable isotope ratio of dissolved inorganic carbon ($\delta^{13}\text{C}_{\text{DIC}}$) and dissolved organic carbon ($\delta^{13}\text{C}_{\text{DOC}}$) using an OI Analytical Aurora 1030 W TOC-TIC analyzer (OI Analytical) coupled in continuous flow mode to a Thermo Scientific Delta V plus isotope ratio mass spectrometer (IRMS). These samples were not acidified to avoid oxidation of the organic carbon. They were reacted with 1 mL of 5% phosphoric acid (H_3PO_4) at 70 °C for 2 min to release the dissolved inorganic carbon (DIC) as CO_2 . The evolved CO_2 was

Table 2 Operating conditions of the ICP-MS measurements

| | |
|----------------------------|--------------------------|
| Plasma power | 1550 W |
| Cool gas flow | 14 L/min |
| Auxiliary gas flow | 0.65 L/min |
| Nebulizer gas flow | 1.03 L/min |
| CCT (KED mode) flow | 5 L/min |
| CCT gas | 8% H_2 in He |
| Sampler/skimmer | material: nickel |
| Spray chamber temperature | 2.7 °C |
| Dwell time | 10 ms (40 ms for Se, As) |
| Number of replicates | 3 |
| RSD (3 replicates) typical | < 1% |
| Number of sweeps | 70 |
| Sample flow | 0.4 ml/min |
| LOD typical | < 0.1 ppb |

purged from the sample by helium. In a second step, 2 mL of 10% sodium persulfate ($\text{Na}_2\text{S}_2\text{O}_8$) was reacted for 5 min at 98 °C to oxidize the DOC to CO_2 and then purged from the solution by helium. A trap and purge (T&P) system was installed to analyze low concentrations. The concentration was determined from the signal of the OI Aurora 1030W internal nondispersive infrared sensor (NDIR) and a set of calibration standards with known concentrations prepared from analytical (A.C.S.) grade potassium hydrogen phthalate (KHP). Areas of the sample peaks are directly proportional to the amount of CO_2 generated by the reaction of the sample with acid (DIC) or sodium persulfate (DOC). The precision (i.e. reproducibility) was better than 5% RSD.

Thermodynamic modeling of the measurements was performed using the software PHREEQC [30]. Simulations of solutions to calculate the solubility curves of sodium sulfates went up to 32 mol/kgw. Solutions with such high ionic strength obviously do not exist in reality, because the sodium sulfate phases precipitate at much lower concentrations. However, they are necessary to obtain a comprehensive result for the solubility curves. Because of this, the pitzer.dat database was used, which is already integrated in the PHREEQC installation. In our calculations, cations and anions change independently from one another. To ensure the electrical neutrality of the solutions, the pH was varied as calculated by PHREEQC.



3 Results

3.1 Raw powder characterization

The raw powder is a synthetic gypsum plaster model mix, partly with natural raw materials, that contains in addition to calcium sulfates several minor phases (Fig. 3). Major phases are bassanite and anhydrite (66 plus 27 wt%). Minor phases are celestine, polyhalite, and anorthite, as well as traces of calcite and quartz (Table 3).

3.2 Efflorescence

During drying, GP samples show efflorescence in the form of a light crust at the edges, that grows significantly when the wetting–drying cycle is repeated (Fig. 4). It first appears at the top of the body, from where it grows downwards. Since external circumstances are not generally controllable and gypsum plasters might be exposed to several drying cycles, even an initially almost unnoticeable efflorescence is not acceptable and needs to be prevented. Yellow–brown stains appear on both, GP and GP–CF prisms, and already appear during the synthesis of the prisms (Fig. 1). However, we have not detected any inconsistencies or extraordinary ion concentrations

Table 3 Phase composition of the raw powder

| Phase | Content (wt%) |
|------------|---------------|
| Bassanite | 66.4 ± 0.5 |
| Anhydrite | 27.3 ± 0.5 |
| Celestine | 2.8 ± 0.3 |
| Polyhalite | 1.2 ± 0.4 |
| Anorthite | 1.7 ± 0.5 |
| Calcite | < 0.5 |
| Quartz | < 0.5 |

during the pore water analysis (chapter 3.5). We thus neglected the appearance of the stains. The GP prism appears slightly brighter.

The focus of investigation in this work remains on the first drying cycle. The foundations for significant efflorescence are laid within this period, and the tendency whether or not the samples will show efflorescence can already be identified on the basis of the pore water measurements. Therefore, all the following experiments were made during the first drying cycle.

3.3 Drying rate

The first drying cycle of the prisms is almost finished after 48 h, and the drying rates of the GP and GP–CF samples are consistent (Fig. 5). The drying process of homogeneous porous media has been the subject of extensive research [31–34]. Two regimes can be distinguished. Within early stages of the drying process, the drying rate is fast and constant. At later stages, the drying rate slows down significantly, which can be attributed to the change from the first to the second regime. In GP and GP–CF this happens after 26–30 h. During the first regime, the pore water network inside the prism is intact; water moves to the outer surface of the prism where it evaporates. Here the limiting factor of the drying rate is the gas transport outside the prism. Once the remaining water in the prism body fills around 20–30% of the pore volume, the water network breaks down and several isolated water clusters develop. During this second drying regime, the water can only move via gas transport. Now the drying rate is limited by this gas transport inside the prism, which is the reason for its deceleration. Dissolved ions can only move towards the surface in liquid water, thus within the first 26 h in the first drying regime. Therefore, efflorescence as well

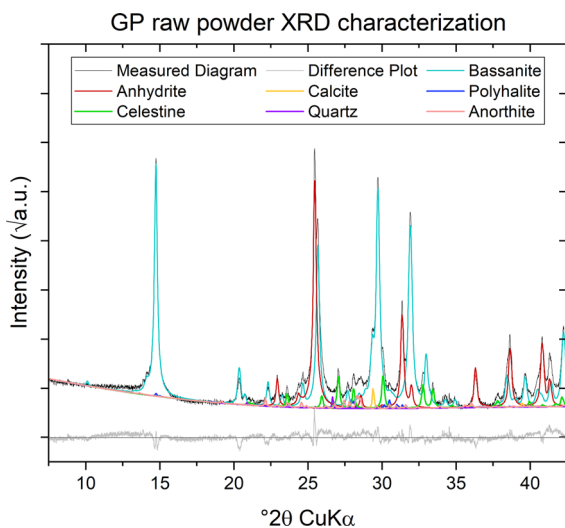


Fig. 3 XRD characterization of the GP raw powder. Intensities are shown in rooted depiction to improve visibility of minor phases

Prism after three drying cycles,
 $T = 23\text{ }^{\circ}\text{C}$, $\text{RH} = 50\%$

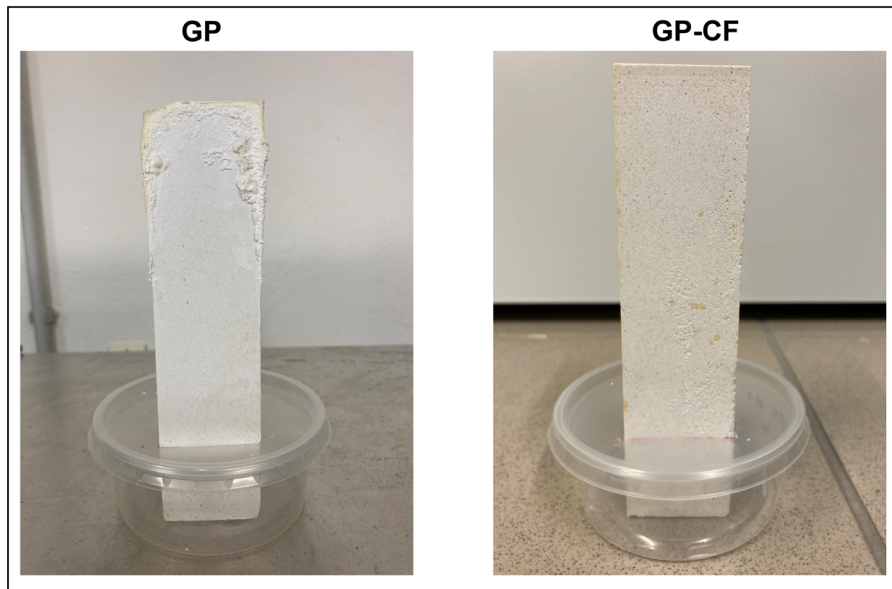


Fig. 4 GP and GP-CF prisms after three drying samples. On GP, significant efflorescence develops. On GP-CF, no efflorescence is visible

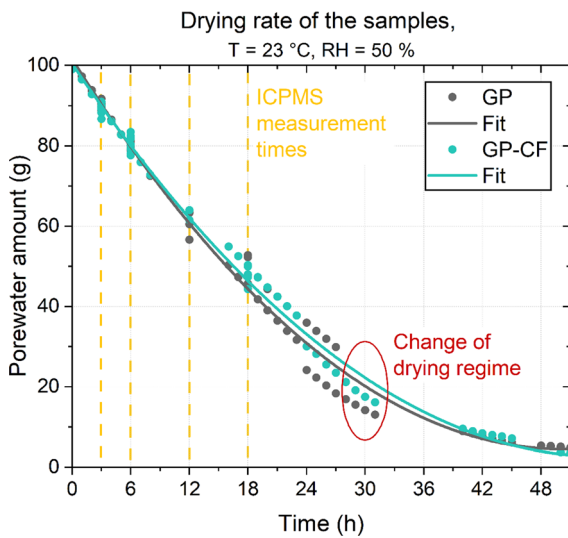


Fig. 5 Drying rate of the GP and GP-CF prism bodies

can only occur within this timeframe. ICP-MS analyses were performed at early measurement times to guarantee that a sufficient amount of pore water could be pressed out of each prism piece.

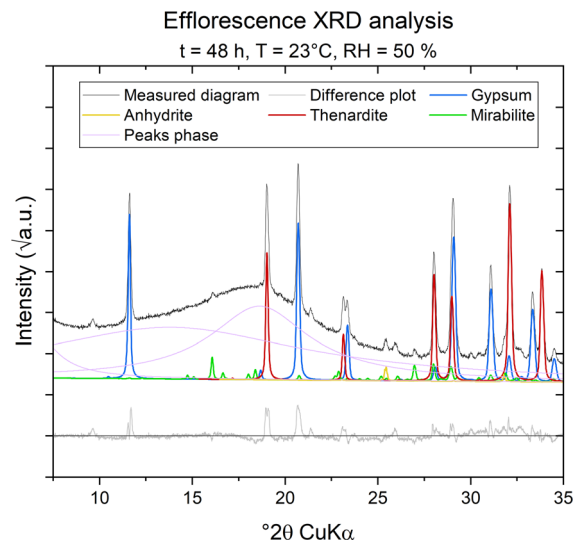


Fig. 6 XRD analysis of the efflorescence scratched off from the GP prism surface. Intensities are shown in rooted depiction to improve visibility of minor phases

3.4 Efflorescence characterization

Figure 6 shows the XRD characterization of the efflorescence on the GP sample. It is almost purely made of sodium sulfates, primarily thenardite in



addition to mirabilite. Gypsum and anhydrite were scratched off from the prism surface as well. The elevated background can be attributed to desiccator grease. To fit the elevation, the background was constrained to 1st Chebichev order before the beginning of the actual analysis of the diffractogram. After the refinement of the mineral phases was finished, a peaks phase was then inserted and refined to get the best fit of the elevated background.

3.5 Pore water composition

Pore water was extracted from all prism pieces after three and six hours of drying time. The concentrations of ions detected in relevant abundance as well as the measured pH values are listed in Table 4. Further measurements of the top prism pieces were performed after 12 and 18 h (Table 5).

The pore water analyses are also depicted in Fig. 7 as a function of the prism height. The background of

Table 5 Ion concentrations in mmol/L of the top prism pieces after 12 and 18 h, measured by ICP-MS

| Time | GP | | GP-CF | |
|--------|------------|------------|-----------|-----------|
| | 12 h | 18 h | 12 h | 18 h |
| Na | 511 ± 75 | 634 ± 63 | 372 ± 38 | 620 ± 21 |
| Mg | 16 ± 4 | 15 ± 2 | 12 ± 1 | 21 ± 3 |
| S | 304 ± 44 | 345 ± 44 | 58 ± 4 | 81 ± 11 |
| K | 58 ± 9 | 60 ± 7 | 40 ± 3 | 67 ± 13 |
| Ca | 15.2 ± 0.2 | 15.0 ± 0.4 | 38 ± 2 | 47 ± 6 |
| Org. C | – | – | 385 ± 52 | 530 ± 20 |
| pH | 9.3 ± 0.3 | 9.2 ± 0.3 | 8.6 ± 0.3 | 8.8 ± 0.3 |

the diagrams show prisms and the respective heights, where they were cut apart. This presentation was chosen for an intuitive display, where the ion trends from the bottom to the prism top are emphasized. Magnesium, potassium, and calcium are relatively

Table 4 Ion concentrations in mmol/L and pH values in the bottom, middle, and top prism pieces after 3 and 6 h

| Time | GP | | GP-CF | |
|---------------|------------|------------|------------|------------|
| | 3 h | 6 h | 3 h | 6 h |
| Na—Bottom | 26 ± 4 | 33 ± 5 | 31 ± 6 | 24 ± 5 |
| | | | 45.0 | |
| | | | 225.01 | |
| Na—Middle | 38 ± 7 | 51 ± 4 | 45 ± 1 | 49 ± 6 |
| Na—Top | 277 ± 29 | 278 ± 3 | 225 ± 36 | 235 ± 11 |
| Mg—Bottom | 0.8 ± 0.1 | 1.2 ± 0.1 | 1.0 ± 0.2 | 0.8 ± 0.1 |
| Mg—Middle | 1.3 ± 0.1 | 1.6 ± 0.1 | 1.3 ± 0.0 | 1.5 ± 0.2 |
| Mg—Top | 7.1 ± 0.3 | 6.8 ± 0.1 | 9 ± 1 | 8.6 ± 0.5 |
| S—Bottom | 26 ± 2 | 31 ± 3 | 23.2 ± 0.7 | 21 ± 1 |
| S—Middle | 32.5 ± 4 | 40 ± 3 | 23.4 ± 0.5 | 25 ± 1 |
| S—Top | 161 ± 16 | 164 ± 4 | 41 ± 2 | 47 ± 3 |
| K—Bottom | 2.8 ± 0.3 | 4.1 ± 0.6 | 5 ± 1 | 3.8 ± 0.3 |
| K—Middle | 4.8 ± 0.6 | 6.5 ± 0.5 | 6.1 ± 0.0 | 6.9 ± 0.6 |
| K—Top | 27 ± 2 | 27 ± 1 | 22 ± 3 | 24 ± 2 |
| Ca—Bottom | 15.0 ± 0.4 | 15.2 ± 0.6 | 18.3 ± 0.4 | 19.3 ± 0.6 |
| Ca—Middle | 14.6 ± 0.4 | 14.6 ± 0.5 | 21.1 ± 0.2 | 22.1 ± 0.5 |
| Ca—Top | 13.3 ± 0.2 | 14.2 ± 0.8 | 32 ± 3 | 29.9 ± 0.5 |
| Org. C—Bottom | – | – | 20 ± 2 | 24 ± 3 |
| Org. C—Middle | – | – | 36 ± 2 | 54 ± 5 |
| Org. C—Top | – | – | 200 ± 38 | 212 ± 35 |
| pH—Bottom | 8.1 ± 0.3 | 8.1 ± 0.3 | 7.8 ± 0.3 | 7.7 ± 0.3 |
| pH—Middle | 8.2 ± 0.3 | 8.2 ± 0.3 | 7.8 ± 0.3 | 7.8 ± 0.3 |
| pH—Top | 8.7 ± 0.3 | 8.6 ± 0.3 | 8.2 ± 0.3 | 8.1 ± 0.3 |



Pore water composition after three and six hours of GP (a and b)), and of GP-CF (c) and d)),

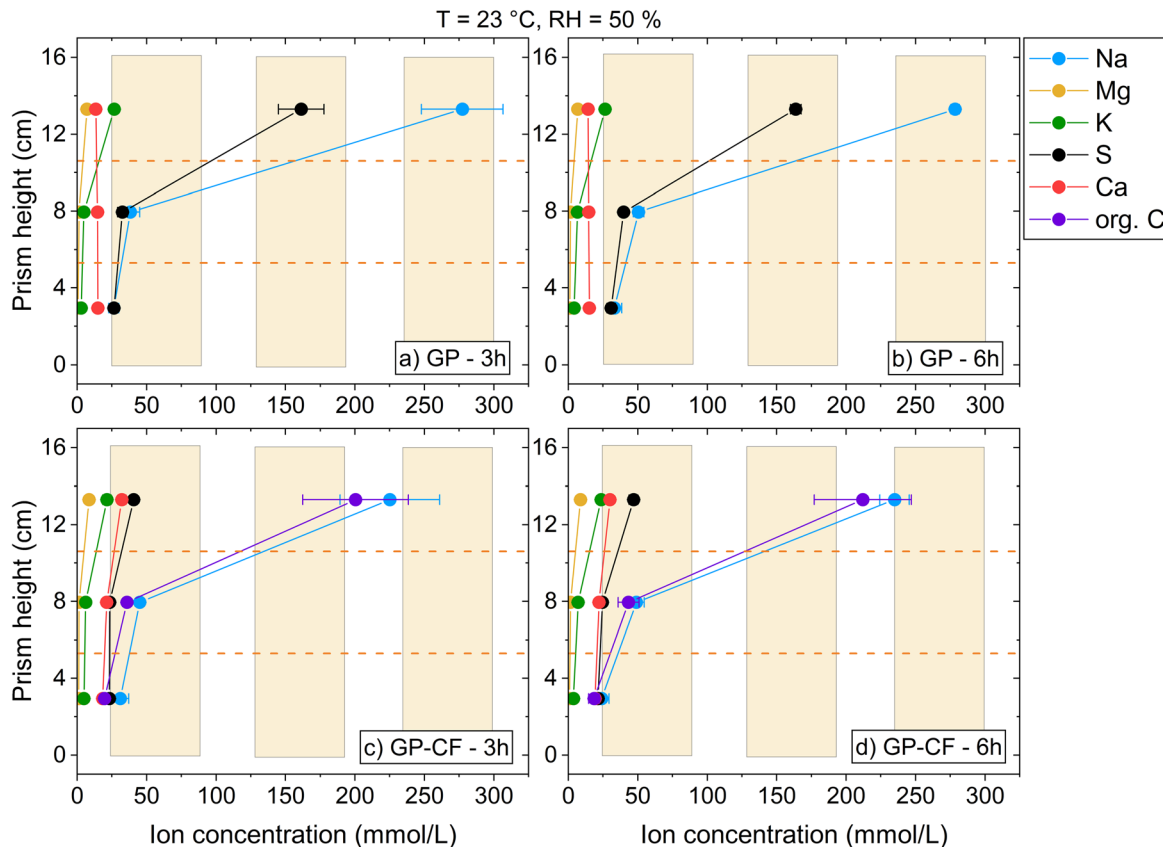


Fig. 7 Pore water analysis after 3 and 6 h as a function of the prism height. **a** and **b** Depict GP, whereas **c** and **d** show GP-CF. Prisms are shown in the background of the data with the respective heights where they were cut apart

equally distributed in the GP sample at concentrations below 50 mmol/L (Fig. 7a and b). Potassium shows slight accumulation in the top piece. Sulfur and sodium concentrations remain constant in the bottom and middle prism pieces. In the top piece, both ions then accumulate strongly to values of more than 150 and 250 mmol/L respectively. The GP-CF sample (Fig. 7c and d) mostly shows the same ion behavior as pure GP. The additional organic carbon follows the trend of sodium and accumulates in the top prism piece. The sodium enrichment at the top reaches values around 225 mmol/L. The important difference compared to the GP sample is the behavior of sulfur. In GP-CF, it follows the trend of calcium and only accumulates slightly at the top. The measured values remain around 50 mmol/L.

From the pore water analysis, it becomes apparent that the top prism pieces are the most relevant ones for further analysis. The ions accumulate there, which

leads to the precipitation of sodium sulfate efflorescence on GP. It is important to note here that the measured concentrations are the average values of the whole pieces. They do not show the exact values at more specific prism heights. In the top third of the prism, the ion accumulation continues with increasing prism height, reaching the highest values at the surface where the water evaporates.

Figure 8 compares the concentrations of the most relevant ions of GP and GP-CF in the top prism piece as a function of time. Differences between GP and GP-CF of the spatial ion distribution are also reflected in the time-dependent ion trends. All ion concentrations remain constant between three and six hours. In the case of GP, sodium and sulfur concentrations both increase afterwards approaching 18 h drying time. In the case of GP-CF, only sodium concentrations increase up to 18 h, whereas sulfur concentrations remain relatively constant throughout the measured

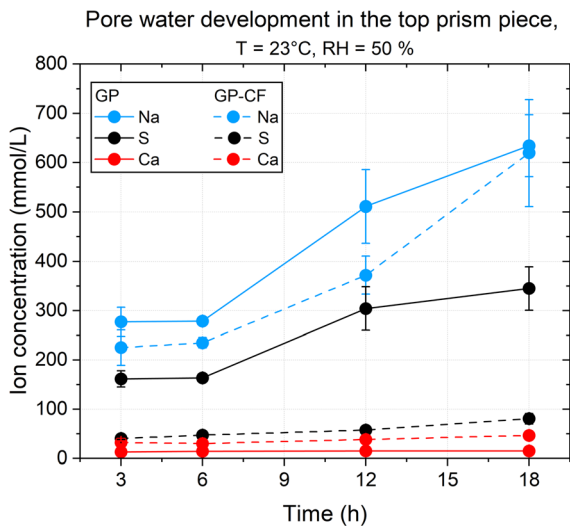


Fig. 8 Concentrations of the most relevant ions in the top prism piece of GP and GP-CF as a function of time

timeframe. Calcium concentrations are low in both samples, but in GP-CF they increase slightly over time (see also Tables 4 and 5).

4 Discussion

4.1 Gypsum equilibrium and Ca/S concentrations

Since gypsum is the main solid phase, its solubility dominates the calcium and sulfur concentrations in the pore water. When the deionized water gets absorbed by the prism and moves upwards, the solid gypsum partially dissolves until calcium and sulfur concentrations in the pore water reaches equilibrium with gypsum. However, its solubility is influenced by the presence of the other ions in the pore water. In general, it increases along with increasing salt concentrations in the solution [35–38]. However, until recently, the influence of alkaline ions on the gypsum solubility as function of its separate ions, calcium and sulfur, has not been calculated. This was first done in [16], and the calculations in this work are based on the same approach. These kinds of calculations are well established in the field of cement research and can lead to important results, as has been demonstrated by [39, 40].

Figure 9 shows the calculated gypsum solubility curves as a function of the Ca/S ratios for the three GP

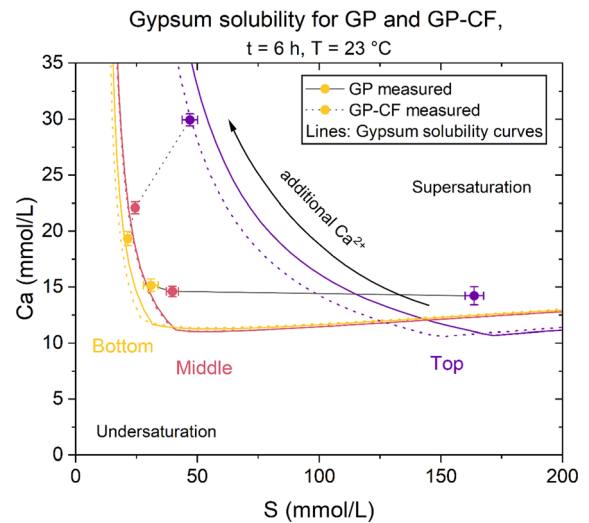


Fig. 9 Comparison of the calculated gypsum solubility (curves) and measured Ca/S ratios (circles) in the prism pieces (bottom, middle, top). GP is depicted by straight lines, and GP-CF by dotted lines. Alkali concentrations of the bottom, middle and top prism piece of the GP sample were 40, 60, and 310 mmol/L respectively. In the GP-CF sample, they were 30, 60, and 270 mmol/L

and GP-CF prism pieces after six hours. The calculations include all detected ions except organic carbon. Measured Ca/S ratios are shown by circles. With increasing prism height, alkali concentrations (majorly sodium) increase as well. In the GP sample, they are 40, 60, and 310 mmol/L in the bottom, middle and top prism piece, respectively. For GP-CF, they are 30, 60, and 270 mmol/L respectively. This leads to a shift in the calculated gypsum solubility to higher sulfur amounts with a constant minimum calcium concentration. Small mismatches of the gypsum solubility curves between the samples at respective heights can be attributed to differences in the alkali concentrations.

The measured Ca/S ion concentrations reflect the solubility change of gypsum towards the top in the GP sample. With increasing prism height, sulfur ions accumulate, whereas calcium ions remain constant at around 15 mmol/L. This can also be seen depending on the drying time in Fig. 8, where between 6 and 18 h only sodium and sulfur concentrations increase. The measured concentrations of each prism piece are always close to the calculated solubility curves of gypsum, slightly in the supersaturation field. This shows that the calcium and sulfur concentrations in the

pore water are controlled by the given gypsum solubility at the respective height.

The Ca/S ion concentrations of the GP-CF sample show another trend. Organic carbon concentrations were not included in this calculation because they are not incorporated in the database. However, the results show again that the measured ion concentrations are in equilibrium with the calculated gypsum solubility curve, as they have to be when water moves through a gypsum body. This implies that the gypsum solubility is not altered significantly by the additional HCOO^- species from CF and that the calculations are true and fair even with the missing information. Although the measured ion concentrations are in equilibrium with gypsum, the Ca/S ratios differ significantly with increasing prism height from GP. The addition of calcium ions by CF leads to their accumulation towards the top. Therefore, lower sulfur concentrations are necessary to reach gypsum equilibrium between pore water and the solid body. This is the main reason why the small CF addition leads to much lower measured sulfur concentrations. The lack of sulfur is replaced by HCOO^- , which maintains the electrical charge balance of the solution. This influences the precipitation of sodium sulfates.

4.2 Sodium sulfate precipitation and Na/S concentrations

In the $\text{Na}_2\text{SO}_4\text{-H}_2\text{O}$ system, mirabilite and thenardite are the only stable mineral phases in air at moderate temperatures. Mirabilite, the decahydrate, occurs at temperatures between 0 and 32 °C and $\text{RH} > 65\%$, whereas thenardite is stable at lower RH [41]. The chosen experimental conditions of this study (23 °C and 50% RH) are in the stability field of thenardite. In a 23 °C solution, however, the solubility of mirabilite is much lower than that of thenardite. Thenardite precipitates directly from solution only at temperatures above 32 °C [41–44]. Previous investigations have however shown that the precipitation of sodium sulfates is also strongly affected by the given RH. At $\text{RH} < 40\%$, thenardite initially precipitates from the solution even at temperatures below 32 °C. Only at $\text{RH} > 40\%$ is mirabilite more likely to form [45, 46]. In recent years, the attention of investigations has focused more on metastable phases. Several authors have reported that during cooling experiments towards temperatures between zero to 15 °C, mirabilite is not

the initial phase that precipitates from solution, but metastable $\text{Na}_2\text{SO}_4\cdot 7\text{H}_2\text{O}$ (heptahydrate) is [41, 47, 48].

Due to the chosen conditions (23 °C and 50% RH), mirabilite is expected to precipitate initially from the pore water in this work. The dehydration to thenardite is a rapid process [49], which is the reason why it was the main detected sodium sulfate phase during the XRD measurement (Fig. 6). Therefore, the thermodynamic calculations initially focus mirabilite. The solubility of thenardite will be taken into account as well afterwards.

The sodium sulfate calculations only comprise the ions sodium and sulfate. Other ions were not included because no significant accumulation towards the top was measured, and small amounts of magnesium, potassium, or calcium have little influence on the sodium sulfate solubility. In the case of organic carbon, the database does not include formate salts, so the carbon again could not be included in the calculations. For the following parts we assume that this has no influence on the sodium sulfate solubility curves. Further calculations in comparison to measured values will later give an indication of the error of our results, and it will be discussed at the end of this chapter. Figure 10a shows the measured Na/S ion ratios of all prisms in the bottom, middle, and top pieces. As can be seen, the ratios increase with linear correlation in all samples with increasing prism height and drying time. This makes it possible to extrapolate the spatial Na/S ion accumulation, thereby simulating the concentrations that may be reached at the top surface of the prism bodies. This can be seen in Fig. 10b together with the calculated solubility curve of mirabilite. The Na/S ratio of the GP sample moves towards the supersaturation field of mirabilite. The phase can precipitate at the surface, where it is visible as efflorescence. If CF is added, the supersaturation of mirabilite is missed due to the sulfur reduction in the pore water.

With the experimental setup of this work, it cannot be measured if the Na/S ion extrapolations remain valid for high ion concentrations, because the highest millimeters of the prisms do not give off enough material to press out pore water. However, this can be verified by further thermodynamic calculations. For this purpose, the gypsum solubility was calculated in the presence of increasing sodium amounts (Fig. 11 a)). Then, the measured Ca/S ion accumulations



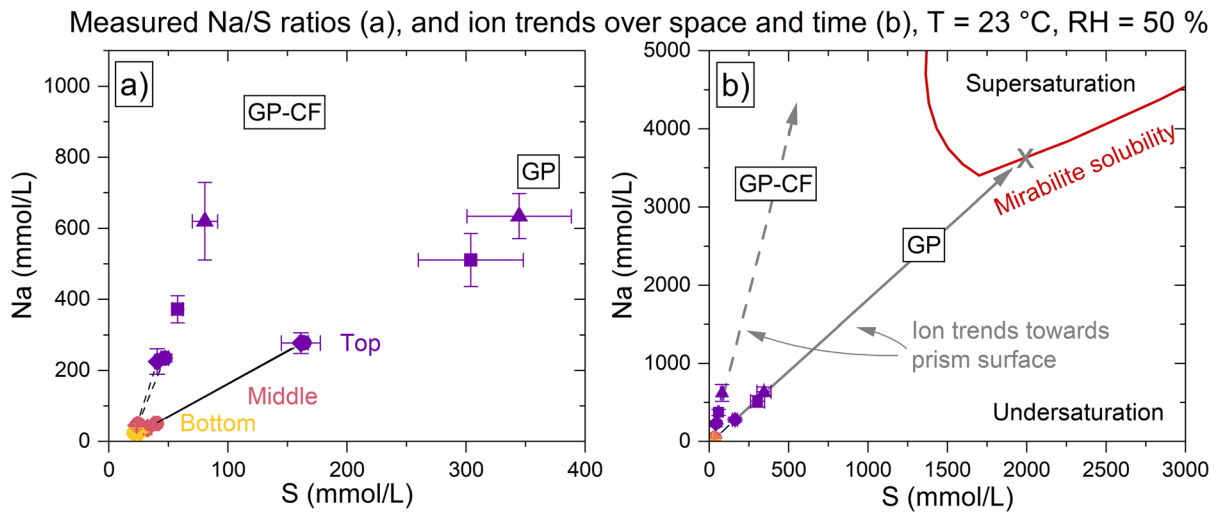


Fig. 10 a Shows measured Na/S ion ratios of the prisms for investigated prism pieces, indicated by the colors. The symbols mark the different drying times: diamonds (◆) represent 3 h, circles (●) 6 h, squares (■) 12 h, and triangles (▲) 18 h.

b Shows the calculated mirabilite solubility together with Na/S ion trends, which were extrapolated from the measured concentrations

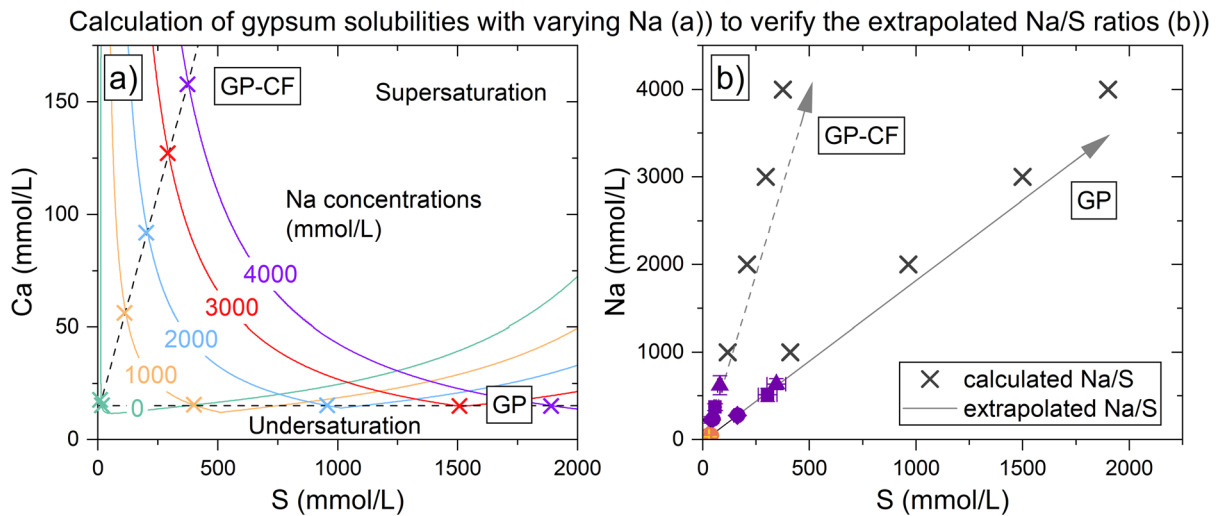


Fig. 11 a Shows the calculated gypsum solubility curves at varying sodium concentrations. Approximations of the spatial Ca/S accumulations of GP and GP-CF, derived from measured concentrations, are shown as well. The crosses mark the Ca/S concentrations, where the modelled ion trends of GP and GP-CF

exceed the calculated equilibrium with gypsum. b Shows the comparison of the measured, calculated, and extrapolated Na/S ratios. The measured Na/S ratios are depicted by the colored symbols (equally to Fig. 10)

shown in Fig. 9 were considered as linear functions (which roughly corresponds to the measured trends) and extrapolated. With their linear formula, the extrapolated calcium and sulfur amounts where the gypsum equilibrium is crossed can be seen in Fig. 11a. These intersection points mark the sodium and sulfur

concentrations, which are in thermodynamic equilibrium with gypsum.

These calculated Na/S ion ratios can now be compared with the trends that were extrapolated from the measured Na/S concentrations of the prisms (Fig. 11b). Given the fact that the measured Ca/S accumulations are not entirely linear and that the



measured values always slightly exceed the calculated gypsum solubility (Fig. 9), the accordance between the Na/S ratios is highly accurate. This shows that the extrapolated ion trends remain true within the whole prism up to the water evaporation front, as long as the thermodynamic equilibrium conditions last. It also indicates once more that the presence of HCOO^- has no significant influence on the solubility of gypsum, underlining the importance of sulfur depletion for preventing the formation of sodium sulfate efflorescence.

The mirabilite solubility calculation of Fig. 10 has been extended to 9 mol/L sodium and 4 mol/L sulfur concentrations, and the solubility curve of thenardite has been added as well (Fig. 12). The modelling estimates that the Na/S trend of GP-CF leads to the formation of thenardite instead of mirabilite after sodium accumulates to approximately 7 mol/L. This is about twice as high as the necessary concentration in the pure GP sample to form mirabilite.

Two possible mechanisms that hinder efflorescence can be derived from these results. The supersaturation of thenardite will be exceeded at some point in the drying process when enough water has evaporated. If this happens within the first drying stage, thenardite will precipitate at the surface. However, contrary to an initial mirabilite precipitation, an initial thenardite precipitation might be invisible. The reason for that is the molar volume difference of 314% between these two phases, due to the incorporation of 10 mol H_2O in

mirabilite. If mirabilite precipitates first, it develops large, visible crystals. Once it transforms into thenardite, the efflorescence remains visible as a curled crust. If thenardite initially precipitates on the surface, however, it might build up as a light white crust that is not visible. However, this explanation seems rather unlikely, given the fact that GP-CF prisms did not show any efflorescence after three drying cycles. The relative humidity near the prism surface is expected to be high due to the evaporation of the pore water. Therefore, if thenardite was present at the surface, it is likely that it would have transformed into mirabilite, which would have again resulted in visible efflorescence.

If the necessary accumulation for thenardite supersaturation is exceeded within the second drying stage, the phase will not precipitate on the surface, but inside the prism body. The reason for this is that the pore water network inside the prism breaks down during the transition from the first to the second drying stage and separate clusters develop. Dissolved ions that remain in the pore water until that point in time are transported into the clusters, where they continue to accumulate due to the continued evaporation of the water until they precipitate.

The discussion so far has been under the assumption that CF does not influence the solubility curves of sodium sulfate phases. This was done because of the lack of thermodynamic information on CF in databases using the Pitzer approach. It is likely, however, that the HCOO^- species compete with sulfate species to form complexes with Na^+ ions in the solution. This would alter the solubility of sodium sulfates to higher ion concentrations, which could also impede the formation of sodium sulfate phases. The extent of this possible influence has not been quantified yet and might play an important role in suppressing the efflorescence. However, it could be shown in this work that the simultaneous depletion of sulfate in the solution is a significant mechanism that hinders sodium sulfate efflorescence formation. The key to the reduction is the dependence of the pore water composition on the solubility of gypsum, which seems not to be influenced strongly by the presence of HCOO^- ions (Fig. 9). Further investigations on this topic with an inclusion of more thermodynamic data will be published in the future.

With every drying cycle, ion accumulations are expected to intensify. This means that CF probably

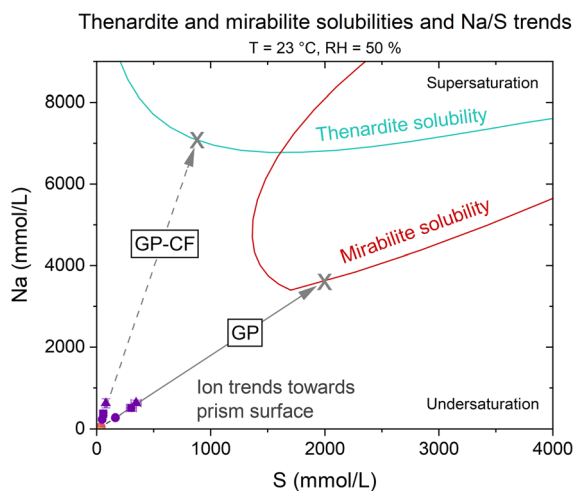


Fig. 12 Solubility curves of the sodium sulfates as function of the Na/S concentrations together with the Na/S ratios of GP and GP-CF after six hours and the respective extrapolations



cannot prevent sodium sulfate efflorescence permanently. If GP–CF is exposed to too many drying cycles, efflorescence is expected to grow on its surface as well. On that same note, it needs to be pointed out again that no efflorescence was visible by naked eye on GP–CF after three drying cycles. CF greatly increases the resistance of the gypsum plaster to sodium sulfate efflorescence at room temperature.

4.3 Formate salt precipitation on GP–CF samples

The question remains what happens to the added calcium formate, since it is a more soluble salt than sodium sulfate. Since the formate replaces sulfate ions in the pore solution, it can be expected that formate salts precipitate at late stages of the drying process. Pore water analyses have shown that the formate is flushed towards the top of the prism, and the formation of formate salts as efflorescence may therefore be an issue that needs to be addressed.

To check whether formate salts can be detected, the surface of a GP–CF sample was scratched off after 48 h of drying and measured by powder diffractometry, similar to the efflorescence characterization (Fig. 13). Formates crystallize on the surface, primarily as calcium formate next to traces of sodium formate. No other formate salts or sodium sulfate

phases were detected. Even after three drying cycles there is no efflorescence visible, which makes the formation of formate salts preferable to sodium sulfate in industrial applications, because no visible “damage” occurs. This reduces complaints from customers and thus costly actions that are otherwise required to remove efflorescence (Fig. 4). In addition to formate, several sulfate salts were detected. Three peaks remain unfitted (at 10.2, 13.8, 25.7 °2θ), which are probably caused by more sulfate solid solution salts. Although the elevated background at 19 °2θ might be attributed to thenardite, its presence cannot be confirmed by X-ray diffraction. Thus it can be concluded, that sodium sulfates primarily grow inside the prism body when CF is added. Usually, subfluorescence is far more damaging for building materials than efflorescence. However, due to the high porosity of gypsum plasters (41–65%), subfluorescence generally does not damage their internal structure, and problems such as fractures have not been observed by naked eye for GP–CF prisms in this study.

5 Conclusions

When the investigated gypsum plaster model dried, sodium sulfate efflorescence developed on its surface. It was possible to prevent this efflorescence formation by adding small amounts of calcium formate. One mechanism of this improved resistance to sodium sulfate efflorescence was discovered by investigating the pore water composition and applying thermodynamic calculations.

The calcium and sulfur concentrations in the pore water are controlled by the solubility of gypsum. Because high amounts of sodium accumulate towards the drying surface, the gypsum solubility is shifted towards higher sulfur amounts. This leads to a simultaneous sulfur accumulation in the pore water. Because of this dependency, sodium sulfates can precipitate on the surface of gypsum plaster bodies.

If calcium formate is added, calcium accumulates towards the drying surface. Due to the higher calcium amounts, less dissolved sulfur is necessary in the pore water to achieve thermodynamic equilibrium with gypsum. Therefore, less sulfur accumulates at the top. Because of this mechanism, the resulting Na/S ratio favors the precipitation of thenardite instead of mirabilite. Also, much higher sodium concentrations

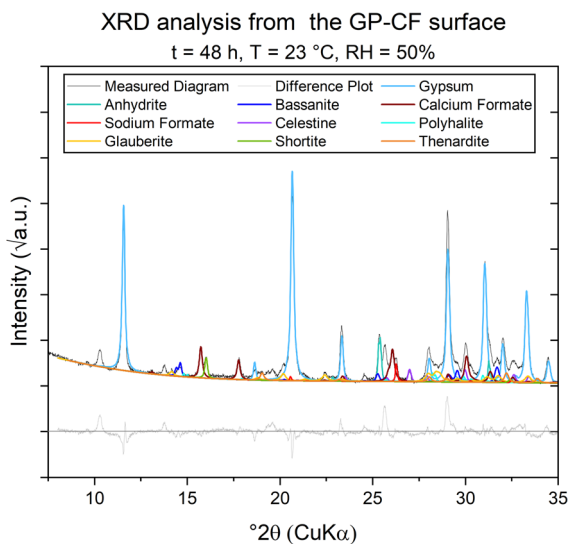


Fig. 13 XRD analysis from the GP–CF surface. Calcium and sodium formate could be detected, but no traces of sodium sulfates were found. Intensities are shown in rooted depiction to improve visibility of minor phases

are necessary for sodium sulfate supersaturation. For this reason, thenardite precipitates at much later drying stages compared to the pure GP sample, probably in the second drying stage. This ensures that thenardite grows inside the prism body and not on its surface. Although formate salts precipitate on the surface of GP-CF, they are not visible even after several drying cycles.

The addition of CF might shift the equilibrium concentrations of sodium sulfate phases to higher values because of the organic carbon accumulation. This could not be checked because thermodynamic information on formate salts is not included in the used database. This might, however, be another important factor for hindering sodium sulfate efflorescence and will be investigated in future research.

Acknowledgements The authors would like to thank Knauf Gips KG for the support of this work as well as Christian Hanke from the Department of Applied Geology for the pore water measurements.

Funding Open Access funding enabled and organized by Projekt DEAL.

Declarations

Conflict of interest The authors declare that they have no known competing financial interests or personal relationships that could have appeared to influence the work reported in this paper.

Open Access This article is licensed under a Creative Commons Attribution 4.0 International License, which permits use, sharing, adaptation, distribution and reproduction in any medium or format, as long as you give appropriate credit to the original author(s) and the source, provide a link to the Creative Commons licence, and indicate if changes were made. The images or other third party material in this article are included in the article's Creative Commons licence, unless indicated otherwise in a credit line to the material. If material is not included in the article's Creative Commons licence and your intended use is not permitted by statutory regulation or exceeds the permitted use, you will need to obtain permission directly from the copyright holder. To view a copy of this licence, visit <http://creativecommons.org/licenses/by/4.0/>.

References

1. Brocken H, Nijland TG (2004) White efflorescence on brick masonry and concrete masonry blocks, with special emphasis on sulfate efflorescence on concrete blocks. *Constr Build Mater* 18:315–323. <https://doi.org/10.1016/j.conbuildmat.2004.02.004>
2. Bishop DL (1934) Function of carbon dioxide in producing efflorescence on plaster and cement products. *J Res Natl Bur Stand* 30(1943):361. <https://doi.org/10.6028/jres.030.026>
3. Zehnder K, Schoch O (2009) Efflorescence of mirabilite, epsomite and gypsum traced by automated monitoring on-site. *J Cult Herit* 10:319–330. <https://doi.org/10.1016/j.culher.2008.10.009>
4. Espinosa-Marzal RM, Scherer GW (2010) Advances in understanding damage by salt crystallization. *Acc Chem Res* 43:897–905. <https://doi.org/10.1021/ar9002224>
5. Caruso F, Wangler T, Flatt RJ (2018) Easy illustration of salt damage in stone. *J Chem Educ* 95:1615–1620. <https://doi.org/10.1021/acs.jchemed.7b00815>
6. Kunther W (2012) Investigation of sulfate attack by experimental and thermodynamic means. *École Polytechnique Fédérale de Lausanne*
7. Coquard P, Boistelle R (1994) Water and solvent effects on the strength of set plaster. *Int J Rock Mech Min Sci Geomech* 31:517–524. [https://doi.org/10.1016/0148-9062\(94\)90153-8](https://doi.org/10.1016/0148-9062(94)90153-8)
8. Scrivener K, Snellings R, Lothenbach B (2018) A practical guide to microstructural analysis of cementitious materials. CRC Press, Boca Raton
9. Flatt RJ, Scherer GW (2002) Hydration and crystallization pressure of sodium sulfate: a critical review. *Mater Res Soc Symp Proc* 712:29–34. <https://doi.org/10.1557/proc-712-ii2.2>
10. Flatt RJ (2002) Salt damage in porous materials: how high supersaturations are generated. *J Cryst Growth* 242:435–454. [https://doi.org/10.1016/S0022-0248\(02\)01429-X](https://doi.org/10.1016/S0022-0248(02)01429-X)
11. Scherer GW (2004) Stress from crystallization of salt. *Cem Concr Res* 34:1613–1624. <https://doi.org/10.1016/j.cemconres.2003.12.034>
12. Heikal M (2004) Effect of calcium formate as an accelerator on the physicochemical and mechanical properties of pozzolanic cement pastes. *Cem Concr Res* 34:1051–1056. <https://doi.org/10.1016/j.cemconres.2003.11.015>
13. Singh NB, Abha K (1983) Effect of calcium formate on the hydration of tricalcium silicate. *Cem Concr Res* 13:619–625. [https://doi.org/10.1016/0008-8846\(83\)90050-9](https://doi.org/10.1016/0008-8846(83)90050-9)
14. Fobbe N, Goetz-Neunhoeffler F, Jansen D (2023) The influence of calcium formate on the hydration of calcium sulfate hemihydrate. *Mater Struct* 56:92. <https://doi.org/10.1617/s11527-023-02181-1>
15. Dinnebier RE, Leineweber A, Evans JSO (2018) Rietveld refinement: practical powder diffraction pattern analysis using TOPAS. *De Gruyter*. <https://doi.org/10.1515/9783110461381>
16. Fobbe N, Goetz-Neunhoeffler F, Foerster H, Foerthner S, Jansen D (2021) Efflorescence during the drying of a technical gypsum body: application of thermodynamic principles. *Constr Build Mater* 303:124445. <https://doi.org/10.1016/j.conbuildmat.2021.124445>
17. Bezou C, Nonat A, Mutin J-C, Christensen AN, Lehmann MS (1995) Investigation of the crystal structure of γ -CaSO₄, CaSO₄ 0.5H₂O, and CaSO₄ 0.6H₂O by powder diffraction methods. *J Solid State Chem* 117:165–176. <https://doi.org/10.1006/jssc.1995.1260>



18. Kirfel A, Will G (1980) Charge density in anhydrite, CaSO_4 , from X-ray and neutron diffraction measurements. *Acta Crystallogr Sect B Struct Crystallogr Cryst Chem* 36:2881–2890. <https://doi.org/10.1107/S0567740880010461>
19. Maslen EN, Streltsov VA, Streltsova NR (1993) X-ray study of the electron density in calcite, CaCO_3 . *Acta Crystallogr Sect B* 49:636–641. <https://doi.org/10.1107/S0108768193002575>
20. Schlatti M, Sahl K, Zemann A, Zemann J (1969) Kristallstruktur von polyhalit, $\text{K}_2\text{Ca}_2\text{Mg}[\text{SO}_4]_4 \cdot 2\text{H}_2\text{O}$. *Naturwissenschaften* 56:368. <https://doi.org/10.1007/BF00596929>
21. Hawthorne FC, Ferguson RB (1975) Anhydrous sulphates. 1: refinement of the crystal structure of celestite with an appendix on the structure of thenadrite. *Can Mineral* 13:181–187
22. Cole WF, Lancucki CJ (1974) A refinement of the crystal structure of gypsum $\text{CaSO}_4 \cdot 2\text{H}_2\text{O}$. *Acta Cryst. B* 30:921–929. <https://doi.org/10.1107/S0567740874004055>
23. Levy HA, Lisensky GC (1978) Crystal structures of sodium sulfate decahydrate (Glauber's salt) and sodium tetraborate decahydrate (borax). Redetermination by neutron diffraction. *Acta Crystallogr Sect B Struct Crystallogr Cryst Chem* 34:3502–3510. <https://doi.org/10.1107/S0567740878011504>
24. Araki T, Zoltai T (1967) Refinement of the crystal structure of a glauberite. *Am Mineral* 52:1272–1277
25. Dickens B, Hyman A, Brown WE (1971) Crystal structure of $\text{Ca}_2\text{Na}_2(\text{CO}_3)_3$. *J Res Natl Bur Stand Sect A Phys Chem* 75A:129. <https://doi.org/10.6028/jres.075a.013>
26. Fuess H, Burger N, Bats JW (1981) Deformationsdichteverteilung in salzen komplexer anionen I: X-N-dichte in α -calciumformiat bei 100 K und 296 K. *Z Krist Cryst Mater* 156:219–232. <https://doi.org/10.1524/zkri.1981.156.3-4.219>
27. Markila PL, Rettig SJ, Trotter J (1975) Sodium formate. *Acta Crystallogr Sect B Struct Crystallogr Cryst Chem* 31:2927. <https://doi.org/10.1107/S0567740875009302>
28. Le Page Y, Donnay G (1976) Refinement of the crystal structure of low-quartz. *Acta Crystallogr Sect B* 32:2456–2459. <https://doi.org/10.1107/S0567740876007966>
29. Wainwright JE, Starkey J (1971) A refinement of the structure of anorthite. *Z Krist Cryst Mater* 133:75–84. <https://doi.org/10.1524/zkri.1971.133.16.75>
30. Parkhurst DL, Appelo CAJ (2013) Description of input and examples for PHREEQC version 3—a computer program for speciation, batch-reaction, one-dimensional transport, and inverse geochemical calculations. U.S. geological survey techniques and methods, book 6, chapter A43, pp 497
31. Huinink HP, Petkovic J, Pel L, Kopinga K (2006) Water and salt transport in plaster/substrate systems. *Heron* 51:9–31
32. Petković J, Huinink HP, Pel L, Kopinga K, Van Hees RPJ (2007) Salt transport in plaster/substrate layers. *Mater Struct Constr* 40:475–490. <https://doi.org/10.1617/s11527-006-9151-7>
33. Le Bray Y, Prat M (1999) Three-dimensional pore network simulation of drying in capillary porous media. *Int J Heat Mass Transf* 42:4207–4224. [https://doi.org/10.1016/S0017-9310\(99\)00006-X](https://doi.org/10.1016/S0017-9310(99)00006-X)
34. Erkselius S, Wadsö L, Karlsson OJ (2008) Drying rate variations of latex dispersions due to salt induced skin formation. *J Colloid Interface Sci* 317:83–95. <https://doi.org/10.1016/j.jcis.2007.09.041>
35. Bock E (1961) On the solubility of anhydrous calcium sulphate and of gypsum in concentrated solutions of sodium chloride. *Can J Chem* 39:1746–1751
36. Wollmann G, Voigt W (2008) Solubility of gypsum in MSO_4 solutions (M = Mg, Mn Co, Ni, Cu, Zn) at 298. 15 K and 313. 15 K. *J Chem Eng Data* 53:1375–1380
37. Ben Ahmed S, Tlili MM, Amami M, Ben Amor M (2014) Gypsum precipitation kinetics and solubility in the $\text{NaCl-MgCl}_2\text{-CaSO}_4\text{-H}_2\text{O}$ system. *Ind Eng Chem Res* 53:9554–9560. <https://doi.org/10.1021/ie5004224>
38. Tanji KK (1969) Solubility of gypsum in aqueous electrolytes as affected by ion association and ionic strengths up to 0.15 m and at 25 °C. *Environ Sci Technol* 3:656–661. <https://doi.org/10.1021/es60030a003>
39. Jansen D, Wolf JJ, Fobbe N (2020) The hydration of nearly pure ye'elimite with a sulfate carrier in a stoichiometric ettringite binder system. Implications for the hydration process based on in-situ XRD, $^1\text{H-TD-NMR}$, pore solution analysis, and thermodynamic modeling. *Cem Concr Res*. <https://doi.org/10.1016/j.cemconres.2019.105923>
40. Zajac M, Skocek J, Bullerjahn F, Lothenbach B, Scrivener K, Ben Haha M (2019) Early hydration of ye'elimite: insights from thermodynamic modelling. *Cem Concr Res* 120:152–163. <https://doi.org/10.1016/j.cemconres.2019.03.024>
41. Steiger M, Asmussen S (2008) Crystallization of sodium sulfate phases in porous materials: The phase diagram $\text{Na}_2\text{SO}_4\text{-H}_2\text{O}$ and the generation of stress. *Geochim Cosmochim Acta* 72:4291–4306. <https://doi.org/10.1016/j.gca.2008.05.053>
42. Tsui N, Flatt RJ, Scherer GW (2003) Crystallization damage by sodium sulfate. *J Cult Herit* 4:109–115. [https://doi.org/10.1016/S1296-2074\(03\)00022-0](https://doi.org/10.1016/S1296-2074(03)00022-0)
43. Blanc P, Lassin A, Piantone P, Azaroual M, Jacquemet N, Fabbri A, Gaucher EC (2012) Thermoddem: a geochemical database focused on low temperature water/rock interactions and waste materials. *Appl Geochem* 27:2107–2116. <https://doi.org/10.1016/j.apgeochem.2012.06.002>
44. Baquerizo LG, Matschei T, Scrivener KL, Saeidpour M, Thorell A, Wadsö L (2014) Methods to determine hydration states of minerals and cement hydrates. *Cem Concr Res* 65:85–95. <https://doi.org/10.1016/j.cemconres.2014.07.009>
45. Rodriguez-Navarro C, Doehne E, Sebastian E (2000) How does sodium sulfate crystallize? Implications for the decay and testing of building materials. *Cem Concr Res* 30:1527–1534. [https://doi.org/10.1016/S0008-8846\(00\)00381-1](https://doi.org/10.1016/S0008-8846(00)00381-1)
46. Rodriguez-Navarro C, Doehne E (1999) Salt weathering: influence of evaporation rate, supersaturation and crystallization pattern. *Earth Surf Process Landf* 24:191–209. [https://doi.org/10.1002/\(sici\)1096-9837\(199903\)24:3%3c191::aid-esp942%3e3.0.co;2-g](https://doi.org/10.1002/(sici)1096-9837(199903)24:3%3c191::aid-esp942%3e3.0.co;2-g)
47. Espinosa Marzal RM, Scherer GW (2008) Crystallization of sodium sulfate salts in limestone. *Environ Geol* 56:605–621. <https://doi.org/10.1007/s00254-008-1441-7>
48. Hamilton A, Hall C (2008) Sodium sulfate heptahydrate: a synchrotron energy-dispersive diffraction study of an



- elusive metastable hydrated salt. *J Anal At Spectrom* 23:840–844. <https://doi.org/10.1039/b716734b>
49. Genkinger S, Putnis A (2007) Crystallisation of sodium sulfate: supersaturation and metastable phases. *Environ Geol* 52:295–303. <https://doi.org/10.1007/s00254-006-0565-x>

Publisher's Note Springer Nature remains neutral with regard to jurisdictional claims in published maps and institutional affiliations.

